Magneto-optical conductivity of monolayer transition metal dichalcogenides in the presence of proximity-induced exchange interaction and external electrical field

Y. Li,[1] Y. M. Xiao,[1, *] W. Xu,[1, 2, 3, †] L. Ding,[1] M. V. Milošević,[4] and F. M. Peeters[4, 3]

[1]*School of Physics and Astronomy and Yunnan Key Laboratory of*
Quantum Information, Yunnan University, Kunming 650091, China
[2]*Key Laboratory of Materials Physics, Institute of Solid State Physics,*
HFIPS, Chinese Academy of Sciences, Hefei 230031, China
[3]*Micro Optical Instruments Inc., Shenzhen 518118, China*
[4]*Department of Physics, University of Antwerp, Groenenborgerlaan 171, B-2020 Antwerpen, Belgium*
(Dated: November 5, 2024)

We theoretically investigate the magneto-optical (MO) properties of monolayer (ML) transition metal dichalcogenides (TMDs) in the presence of external electrical and quantizing magnetic fields and of the proximity-induced exchange interaction. The corresponding Landau Level (LL) structure is studied by solving the Schrödinger equation and the spin polarization in ML-TMDs under the action of the magnetic field is evaluated. The impact of trigonal warping on LLs and MO absorption is examined. Furthermore, the longitudinal MO conductivity is calculated through the dynamical dielectric function under the standard random-phase approximation (RPA) with the Kubo formula. We take ML-MoS$_2$ as an example to examine the effects of proximity-induced exchange interaction, external electrical and magnetic fields on the MO conductivity induced via intra- and interband electronic transitions among the LLs. For intraband electronic transitions within the conduction or valence bands, we can observe two absorption peaks in terahertz (THz) frequency range. While the interband electronic transitions between conduction and valence LLs show a series of absorption peaks in the visible range. We find that the proximity-induced exchange interaction, the carrier density, the strengths of the external electrical and magnetic fields can effectively modulate the positions of the absorption peaks and the shapes of the MO absorption spectra. The results obtained from this study can benefit to an in-depth understanding of the MO properties of ML-TMDs which can be potentially applied for magneto-optic, spintronic and valleytronic devices working in visible to THz frequency bandwidths.

I. INTRODUCTION

Since the discovery of graphene in 2004 [1], the investigation of atomically thin or two-dimensional (2D) electronic materials has become an important and fast-growing field of research field in condensed matter physics and electronics. In recent years, monolayer (ML) transition metal dichalcogenides (TMDs) have attracted a great attention due to their excellent and unique physical properties such as the spintronic and valleytronic features for potential applications in, e.g., information technology. From a viewpoint of condensed matter physics, ML-TMDs is in the form of X-M-X with two layers of chalcogen atoms (X=S, Se, Te) in two hexagonal planes separated by a plane of metal atoms (M=Mo, W, Nb, Ta, Ti) [2]. ML-TMDs has the direct band gaps around the K- and K'-point, whereas the multi-layer TMDs are normally with indirect gaps [3, 4]. Due to the presence of the intrinsic spin and the Rashba spin-orbit coupling (SOC), the spin degeneracy in ML-TMDs is often lifted and the spin orientations in energy states in different valleys are just opposite. The corresponding spin polarization can be observed experimentally by using, e.g., optical measurements with circularly polarized radiation

field [5, 6]. Moreover, it has been found that the valley degeneracy in ML-TMDs can be lifted via, e.g., introducing the exchange interaction induced by, e.g., the proximity effect in the presence of ferromagnetic substrate [7–9]. Therefore the spin-orbit and spin-valley couplings in ML-TMDs can contribute to the unique spin and valley degree of freedoms. As a result, ML-TMDs can be applied as spin and valley filter [10], gas-sensor [11], ultrasensitive photodetectors [12], and field-effect transistors (FETs) with on/off ratios of the order of 10^8 and mobility larger than 200 cm^{2}V^{-1}s^{-1}[13]. These interesting characteristics suggest that ML-TMDs based 2D electronic materials are promising candidates for next generation of high performance devices in nano-electronics [14], optoelectronics [15, 16], twistronics [17], spintronics and valleytronics [5, 18–20].

The investigation of the electronic and optoelectronic properties of two dimensional electron gas (2DEG) in the presence of an external magnetic field is an intriguing field of research [21–25]. More specifically, the magneto-optical (MO) properties of ML-TMDs have attracted lots of attentions in recent years [26–29]. When a quantizing magnetic field is applied perpendicularly to the 2D plane of a ML-TMDs, the Landau quantization can lead to the Landau levels (LLs) in the energy spectrum and the electronic transitions among these LLs can result in many interesting physical phenomena such as the integer quantum Hall effect [30, 31], fractional quan-

tum Hall effect [32], Shubnikov-de Haas (SdH) oscillations [33, 34], photo-induced anomalous Hall effect [35], etc. As we know, the MO conductivity is a key physical quantity which is directly related to the MO absorption measured experimentally via transmission and reflection. The theoretical calculation of MO conductivity of ML-TMDs was carried out by taking into account of spin and valley polarizations, electron-phonon coupling, spin and valley Zeeman effects, and nonlinear effect [30, 31, 36–38]. It has been shown that the spin and valley dependent MO absorption induced by the electronic transitions among LLs can occur in visible to terahertz (THz) bandwidth. These unique and interesting MO properties of ML-TMDs can be utilized to design and apply for the advanced MO materials and devices for applications from visible to THz bandwidths.

Moreover, due to the unique feature of light-valley coupling [39, 40], ML-TMDs can exhibit the novel transport effects such as valley-selective circular dichroism [20], valley Hall effect (VHE) [5], and Faraday rotation [41]. The enhancement of valley splitting and a large valley polarization of ML-TMDs can be achieved through placing it on ferromagnetic substrate such as EuO via the proximity-induced exchange interaction [7, 8]. The techniques for tuning the spin and/or valley degree of freedoms of ML-TMDs are prominent research fields for the time being. It should be noted that the proximity-induced exchange interaction can lift the valley degeneracy in electronic energy spectrum in ML-TMDs. Apparently, the optical [9] and MO properties of ML-TMDs can be affected by the lifting of the valley degeneracy. Thus, it is interesting and significant to investigate the MO properties of ML-TMDs with the breaking of the spin and valley degeneracies by the proximity-induced exchange interaction. This becomes the prime motivation of this study. In this work, we study theoretically the Landau level structure and the longitudinal MO conductivity of both n-type and p-type ML-TMDs in the presence of proximity-induced exchange interaction which can be induced by the substrate together with external electrical and magnetic fields. The effects of spin and valley polarizations, magnetic field strength, electrical field strength, proximity-induced exchange interaction, and carrier density on the MO conductivity of ML-MoS$_2$ are examined theoretically.

The present paper is organized as follows. In Sec. II, we evaluate the LL structure and the longitudinal magneto-optical conductivity of both n-type and p-type ML-TMDs with the framework of dynamical dielectric function on the basis of the random-phase approximation (RPA). In Sec. III, we analyze and discuss the influence of spin and valley polarizations on MO conductivity induced by electronic transitions within the conduction/valence LLs and between the conduction and valence LLs in ML-TMDs such as ML-MoS$_2$. The main conclusions obtained from this study are summarized in Sec. IV.

II. THEORETICAL APPROACH

A. Landau level structure

We consider a ML-TMDs laid in the x-y plane on a ferromagnetic substrate which can lead to an exchange interaction in the presence of an external perpendicular electrical field $\mathbf{E} = (0, 0, E_z)$. The Hamiltonian for an electron in ML-TMDs at K (K') valley can be written as [7, 9, 38, 42]

$$H^\zeta(\mathbf{k}) = \hbar v_{\mathrm{F}}(\zeta k_x \hat{\sigma}_x + k_y \hat{\sigma}_y) + (\Delta + edE_z)\hat{\sigma}_z \\ + \zeta s(\lambda_c \hat{\sigma}_+ + \lambda_v \hat{\sigma}_-) - s(B_c \hat{\sigma}_+ + B_v \hat{\sigma}_-), \quad (1)$$

where $\mathbf{k} = (k_x, k_y)$ is the carrier wave vector or momentum operator, v_{F} is the Fermi velocity, $\zeta = \pm 1$ is the index for K (K') valley, $s = \pm 1$ is a good quantum number for spin up/down states (implying that the spin-flip transitions are prohibited in the system), $\hat{\sigma}_i$ and $\hat{s}_i$ are the Pauli matrices of the sublattice pseudo-spin and the real spin respectively, $\hat{\sigma}_0$ is an unit 2×2 identity matrix, $\hat{\sigma}_\pm = (\hat{\sigma}_0 \pm \hat{\sigma}_z)/2$, Δ is the band gap parameter of the ML-TMDs, $2d$ is the vertical distance between the M (e.g., Mo) and X (e.g., S) sublattices in ML-TMDs, and E_z is the strength of the applied perpendicular electrical field. We note that the term $edE_z\hat{\sigma}_z$ is induced on the basis of the fact that the conduction and valence band edges near K and K' points in ML-TMDs are attributed mainly from d_{z^2}, d_{xy} and $d_{x^2-y^2}$ orbits of the metal atoms. The thickness of the ML-TMD is $4d$. In Eq. (1), λ_c and λ_v are the intrinsic spin-orbit coupling (SOC) parameters in conduction and valence band. B_c and B_v are the experienced effective Zeeman fields originated from the proximity-induced exchange interaction in conduction and valence bands, respectively. It should be noted that the parameters B_c and B_v should depend on the band alignment between the TMDs layer and the ferromagnetic substrate and on the surface termination of the substrate. They can be obtained through, e.g., ab initio calculations [7, 43]. In the present study, we take B_c and B_v as the input parameters in the following calculations. Furthermore, the band gap parameter Δ is always present in ML-TMDs. As we can see from the second term on the righthand side of Eq. (1), the actual band gap in ML-TMDs in the presence of pseudo-spin induced by Pauli matrix σ_z can be affected by the presence of the perpendicular electric field E_z. This Hamiltonian can also be written in the form of a matrix

$$H^\zeta = \begin{pmatrix} \Delta_{\zeta s} & \zeta \hbar v_{\mathrm{F}} k_{-\zeta} \\ \zeta \hbar v_{\mathrm{F}} k_\zeta & -\Delta_{\zeta s} \end{pmatrix} + O_{\zeta s}, \quad (2)$$

where $k_\pm = k_x \pm ik_y = ke^{\pm i\theta}$, θ is the angle between $\mathbf{k}$ and the x axis, and $O_{\zeta s} = \zeta s(\lambda_c + \lambda_v)/2 - s(B_c + B_v)/2$. The corresponding Schrödinger equation can be solved analytically and the eigenvalues are obtained as

$$\varepsilon_\beta^{\zeta s}(\mathbf{k}) = \beta\sqrt{\hbar^2 v_{\mathrm{F}}^2 k^2 + \Delta_{\zeta s}^2} + O_{\zeta s}, \quad (3)$$

where $\Delta_{\zeta s} = \Delta + \zeta s(\lambda_c - \lambda_v)/2 - s(B_c - B_v)/2 + edE_z$ with $\beta = \pm 1$ refers to conduction and valence band, respectively.

In the presence of a perpendicular magnetic field $\mathbf{B} = (0, 0, B)$ applied in the Faraday geometry on a ML-TMDs layer, the Hamiltonian for an electron in ML-TMDs now becomes [7, 9, 30, 38]

$$H^\zeta = v_F(\zeta\Pi_x\hat{\sigma}_x + \Pi_y\hat{\sigma}_y) + (\Delta + edE_z)\hat{\sigma}_z$$
$$+ \zeta s(\lambda_c\hat{\sigma}_+ + \lambda_v\hat{\sigma}_-) - s(B_c\hat{\sigma}_+ - B_v\hat{\sigma}_-)$$
$$+ sM_s - \zeta M_v. \quad (4)$$

Here, $\mathbf{\Pi} = \mathbf{p} + e\mathbf{A}$ is the canonical momentum with a vector potential $\mathbf{A}$, $M_j = g_j\mu_B B/2$, the Bohr magneton $\mu_B = e\hbar/2m_e$ with m_e being the rest electron mass, $j = s, v$ stands for the spin or valley Zeeman field, $g_s = g_e + g'_s$, $g_e = 2$ is the g-factor for an free-electron, and g'_s is out-of-plane effective spin g-factor due to the presence of the SOC [30, 44]. We have taken the Landau gauge $\mathbf{A} = (0, Bx, 0)$ for the vector potential of the magnetic field for the theoretical calculation in this study.

After defining the ladder operators with the magnetic field, $a_\pm = l(\Pi_x \pm i\Pi_y)/(\sqrt{2}\hbar)$ which acts on the wave functions of the harmonic oscillator and $l = \sqrt{\hbar/eB}$ is the magnetic length, the Hamiltonian given by Eq. (4) can be written as

$$H^\zeta = \begin{pmatrix} \Delta_{\zeta s} & \zeta\hbar\omega_c a_\mp \\ \zeta\hbar\omega_c a_\pm & -\Delta_{\zeta s} \end{pmatrix} + O_{\zeta s} + sM_s - \zeta M_v, \quad (5)$$

where $\omega_c = \sqrt{2}v_F/l$ is the cyclotron frequency for a ML-TMDs system. After diagonalizing this Hamiltonian, we obtain the electronic energy for a state $\alpha = (\zeta, s, \beta, n, k_y)$ as

$$E_\alpha = E_{\beta n}^{\zeta s} = \beta h_n^{\zeta s} + O_{\zeta s} + sM_s - \zeta M_v, \quad (6)$$

where $h_n^{\zeta s} = [n\hbar^2\omega_c^2 + \Delta_{\zeta s}^2]^{1/2}$ and n is the LL index. The corresponding eigenfunctions $\psi_{\beta n k_y}^{\zeta s}$ for the K and K' valleys are given respectively by [30]

$$\psi_{\beta n k_y}^{+s} = \frac{e^{ik_y y}}{\sqrt{L_y}}\begin{pmatrix} C_{\beta n}^{+s}\phi_{n-1}(\overline{x}) \\ D_{\beta n}^{+s}\phi_n(\overline{x}) \end{pmatrix}, \quad (7)$$

and

$$\psi_{\beta n k_y}^{-s} = \frac{e^{ik_y y}}{\sqrt{L_y}}\begin{pmatrix} -C_{\beta n}^{-s}\phi_n(\overline{x}) \\ D_{\beta n}^{-s}\phi_{n-1}(\overline{x}) \end{pmatrix}. \quad (8)$$

Here, the normalization constants are $C_{\beta n}^{\zeta s} = [1/2 + \beta\Delta_{\zeta s}/(2h_n^{\zeta s})]^{1/2}$ and $D_{\beta n}^{\zeta s} = [1/2 - \beta\Delta_{\zeta s}/(2h_n^{\zeta s})]^{1/2}$, k_y is the electron wave vector along the y direction, $\overline{x} = x - x_0$ with $x_0 = l^2 k_y$, and $\phi_n(x) = e^{-x^2/2}H_n(x)/\sqrt{2^n n!\sqrt{\pi}l}$ with $H_n(x)$ being the Hermite polynomials. Specially, the eigenfunctions for $n = 0$ at the K and K' valleys are given respectively as

$$\psi_{\beta 0 k_y}^{+s} = \frac{e^{ik_y y}}{\sqrt{L_y}}\begin{pmatrix} 0 \\ \phi_0(\overline{x}) \end{pmatrix} \text{ and } \psi_{\beta 0 k_y}^{-s} = \frac{e^{ik_y y}}{\sqrt{L_y}}\begin{pmatrix} \phi_0(\overline{x}) \\ 0 \end{pmatrix}. \quad (9)$$

B. Effect of trigonal warping

In the presence of an external magnetic field, the trigonal warping can lead to higher-order corrections to electronic band structure in ML-TMD. This effect can be accounted via the term [26, 45]

$$H_{tw}^\zeta = -\frac{2\gamma}{l^2}\begin{pmatrix} 0 & a_\pm^2 \\ a_\mp^2 & 0 \end{pmatrix}, \quad (10)$$

where the relevant parameter $\gamma = -1.02$ eVÅ^2 is associated with the trigonal warping and can be obtained from fitting of the energy spectra to tight-binding or ab initio calculations [26, 45]. By using the perturbation theory, we can take the trigonal warping as a second-order correction relative to the leading LLs. For the K and K' valleys, the second-order corrections $E_\alpha^{(2)}$ are given respectively as

$$E_\alpha^{(2)} = \frac{4\gamma^2}{l^4}[\mathbb{A}_{n\beta}^{+s}C_{\beta n+3}^{+s}D_{\beta n}^{+s}\sqrt{(n+1)(n+2)}$$
$$+ \mathbb{B}_{n\beta}^{+s}C_{\beta n}^{+s}D_{\beta n-3}^{+s}\sqrt{(n-1)(n-2)}], \quad (11)$$

with $\mathbb{A}_{n\beta}^{+s} = C_{\beta n+3}^{+s}D_{\beta n}^{+s}\sqrt{(n+1)(n+2)}/(E_{\beta n}^{+s} - E_{\beta n+3}^{+s})$ and $\mathbb{B}_{n\beta}^{+s} = C_{\beta n}^{+s}D_{\beta n-3}^{+s}\sqrt{(n-1)(n-2)}/(E_{\beta n}^{+s} - E_{\beta n-3}^{+s})$, and

$$E_\alpha^{(2)} = \frac{4\gamma^2}{l^4}[\mathbb{A}_{n\beta}^{-s}C_{\beta n}^{-s}D_{\beta n+3}^{-s}\sqrt{(n+1)(n+2)}$$
$$+ \mathbb{B}_{n\beta}^{-s}C_{\beta n-3}^{-s}D_{\beta n}^{-s}\sqrt{(n-1)(n-2)}], \quad (12)$$

with $\mathbb{A}_{n\beta}^{-s} = C_{\beta n}^{-s}D_{\beta n+3}^{-s}\sqrt{(n+1)(n+2)}/(E_{\beta n+3}^{-s} - E_{\beta n}^{-s})$ and $\mathbb{B}_{n\beta}^{-s} = C_{\beta n-3}^{-s}D_{\beta n}^{-s}\sqrt{(n-1)(n-2)}/(E_{\beta n-3}^{-s} - E_{\beta n}^{-s})$. The modified eigenstate $\psi_\alpha^{(1)}$ with the first order at K and K' valleys are given respectively by

$$\psi_\alpha^{(1)} = -\frac{2\gamma}{l^2}(\mathbb{A}_{n\beta}^{+s}\psi_{\beta,n+3,k_y}^{+s} + \mathbb{B}_{n\beta}^{+s}\psi_{\beta,n-3,k_y}^{+s}), \quad (13)$$

and

$$\psi_\alpha^{(1)} = -\frac{2\gamma}{l^2}(\mathbb{A}_{n\beta}^{-s}\psi_{\beta,n+3,k_y}^{-s} + \mathbb{B}_{n\beta}^{-s}\psi_{\beta,n-3,k_y}^{-s}). \quad (14)$$

The total eigenfunction is

$$\psi_\alpha' = \mathbb{F}(\psi_{\beta n k_y}^{\zeta s} + \psi_\alpha^{(1)}), \quad (15)$$

with $\mathbb{F} = l^2/\{l^4 + 4\gamma^2[(\mathbb{A}_{n\beta}^{\zeta s})^2 + (\mathbb{B}_{n\beta}^{\zeta s})^2]\}^{1/2}$ being the normalization factor. The effect of trigonal warping can result in additional allowed transition channels $n \to n \pm 2$ and $n \to n \pm 4$. However, it has been shown that the spectral weights of the magneto-optical absorption spectra induced by trigonal warping is significantly lower than those induced by the usual dipolar transitions [26].

C. Density-of-states and spin-polarization

The density-of-states (DOS) per unit area can be obtained through the imaginary part of the Green's function via

$$D(E) = \frac{1}{S_0} \sum_{\zeta,s,n,k_y} \text{Im } G_\alpha(E),\qquad(16)$$

where $G_\alpha(E) = (E - E_\alpha + i\delta)^{-1}$ is the retarded Green's function, E is the carrier energy, and S_0 the area of the sample system. With the non-degenerate statistics in our system, the summation over k_y can be replaced by an integration [30, 31]

$$\sum_{k_y} \to \frac{L_y}{2\pi} \int_{-k_0}^{k_0} dk_y = \frac{S_0}{D_0},\qquad(17)$$

where $k_0 = L_x/(2l)^2$ and $D_0 = 2\pi l^2$. Therefor, Eq. (16) can also be written as

$$D(E) = \frac{1}{D_0} \sum_{\zeta,s,n} \delta(E - E_{\beta n}^{\zeta s}).\qquad(18)$$

At a finite temperature, the electron (hole) density n_β ($\beta = +$ for electrons in conduction band and $\beta = -$ for holes in valence band) satisfies the electron number conservation law [6, 30]

$$n_\beta = \frac{1}{D_0} \sum_{\zeta,s,n} [\delta_{\beta,-1} + \beta f(E_{\beta n}^{\zeta s})],\qquad(19)$$

where $f(x) = [1+\exp((x-\mu_\beta)/(k_BT))]^{-1}$ is Fermi-Dirac function with μ_β being the chemical potential (or Fermi energy E_F at zero temperature) for electrons in n-type or holes in p-type sample. The spin polarization of the system is given by

$$\mathcal{S} = \frac{n_\beta^{++} + n_\beta^{-+} - n_\beta^{+-} - n_\beta^{--}}{n_\beta},\qquad(20)$$

where $n_\beta = n_\beta^{++} + n_\beta^{-+} + n_\beta^{+-} + n_\beta^{--}$, and $n_\beta^{\zeta s} = \sum_n [\delta_{\beta,-1} + \beta f(E_{\beta n}^{\zeta s})]/D_0$.

D. Dynamical RPA dielectric function and magneto-optical conductivity

In this study, we study the MO properties of ML-TMDs in the presence of quantizing magnetic field under the standard random phase approximation (RPA). The PRA approach has been successfully employed in studying the collective excitations in 2DEG systems in the presence or absence of an external magnetic field [24, 46–50]. The dynamical RPA dielectric function for ML-TMDs can be written as

$$\epsilon(q,\omega) = 1 - v_c(q)\Pi(q,\omega),\qquad(21)$$

where $v_c(q) = 2\pi e^2/\kappa q$ is the 2D Fourier transform of the Coulomb potential, κ the effective background dielectric constant of ML-TMDs, and $\mathbf{q} = (q_x, q_y)$ is the change of the electron wavevector during an electron-electron (e-e) scattering event. The non-interacting density-density (d-d) correlation function is given by [51]

$$\Pi(q,\omega) = \frac{1}{S_0} \sum_{\zeta,s} \sum_{\beta n,\beta' n'} \sum_{k_y,k_y'} \mathbb{C}_{\beta n k_y, \beta' n' k_y'}^{\zeta s}(q)$$
$$\times \frac{f(E_{\beta n}^{\zeta s}) - f(E_{\beta' n'}^{\zeta s})}{E_{\beta n}^{\zeta s} - E_{\beta' n'}^{\zeta s} + \hbar\omega + i\delta},\qquad(22)$$

where the form factor for e-e interaction is

$$\mathbb{C}_{\beta n k_y, \beta' n' k_y'}^{\zeta s}(q) = |\langle\alpha'|e^{-i\mathbf{q}\cdot\mathbf{r}}|\alpha\rangle|^2 = V_{\beta n,\beta' n'}^{\zeta s}(u)\delta_{k_y', k_y - q_y},$$

and

$$V_{\beta n,\beta' n'}^{\zeta s}(u) = [C_{\beta',n'}^{\zeta s} C_{\beta,n}^{\zeta s} F_{n-1,n'-1}(u)$$
$$+ D_{\beta',n'}^{\zeta s} D_{\beta,n}^{\zeta s} F_{n,n'}(u)]^2,\qquad(23)$$

with $u = l^2 q^2/2$. For $n \le n'$, we have $[F_{n,n'}(u)]^2 = [n!/n'!]e^{-u}u^{n'-n}[L_n^{n'-n}(u)]^2$ and $L_N^J(x)$ is the Laguerre polynomial. For the case of $n > n'$, it has the same expression but with that n and n' are interchanged. We expand $V_{\beta n,\beta' n'}^{\zeta s}(u)$ to the lowest order ($n'-n = \pm 1$) with

$$V_{\beta n,\beta' n+1}^{\zeta s}(u) \to [C_{\beta' n+1}^{\zeta s} C_{\beta n}^{\zeta s}]^2 nu + [D_{\beta' n+1}^{\zeta s} D_{\beta n}^{\zeta s}]^2(n+1)u$$
$$+ 2C_{\beta' n+1}^{\zeta s} C_{\beta n}^{\zeta s} D_{\beta' n+1}^{\zeta s} D_{\beta n}^{\zeta s}[n(n+1)]^{1/2}u,\qquad(24)$$

and

$$V_{\beta n,\beta' n-1}^{\zeta s}(u) \to [C_{\beta' n-1}^{\zeta s} C_{\beta n}^{\zeta s}]^2(n-1)u + [D_{\beta' n-1}^{\zeta s} D_{\beta n}^{\zeta s}]^2 nu$$
$$+ 2C_{\beta' n-1}^{\zeta s} C_{\beta n}^{\zeta s} D_{\beta n-1}^{\zeta s} D_{\beta n}^{\zeta s}[n(n-1)]^{1/2}u,\qquad(25)$$

respectively. The real part of the longitudinal MO conductivity for a 2D electronic system can be derived from the Kubo formula [52], which reads

$$\sigma_{xx}(\omega) = \lim_{q\to 0} \frac{\kappa\omega}{2\pi q}\text{Im } \epsilon(\omega,q) = -\lim_{q\to 0} \frac{e^2\omega}{q^2}\text{Im }\Pi(q,\omega).\qquad(26)$$

The real and imaginary parts of the (d-d) correlation function can be obtained from the Dirac identity

$$\lim_{\eta\to 0^+} \frac{1}{x \pm i\eta} = \mathcal{P}(\frac{1}{x}) \mp i\pi\delta(x),\qquad(27)$$

where $\mathcal{P}$ denotes the principal value of $1/x$. Therefore the longitudinal MO conductivity is obtained as

$$\sigma_{xx}(\omega) = \lim_{q\to 0} \frac{\pi\sigma_0\hbar\omega}{2u} \sum_{\zeta,s,n,\beta,\beta'} \delta_{n',n\pm 1}[f(E_{\beta n}^{\zeta s}) - f(E_{\beta' n'}^{\zeta s})]$$
$$\times V_{\beta n,\beta' n'}^{\zeta s}\delta(E_{\beta n}^{\zeta s} - E_{\beta' n'}^{\zeta s} + \hbar\omega),\qquad(28)$$

where $n' = n \pm 1$ is given by the selective rules for electronic transitions and $\sigma_0 = e^2/h$ is the quantum conductivity.

In the present study, we mainly focus on the magneto-optical response of ML-TMDs by looking into the real part of the longitudinal MO conductivity $\sigma_{xx}(\omega)$. From the obtained RPA dielectric function, we can also evaluate the imaginary part of the longitudinal MO conductivity. It is known that the real part of the optical conductivity corresponds to the energy-consuming process or optical absorption, whereas the imaginary part of it describes the energy exchanging process between electrons and the radiation field. It should be noted that the dynamical dielectric function and the corresponding MO conductivity obtained in this study are the consequence of the density-density correlation induced by e-e interaction. They correspond to the diagonal components of the dynamical dielectric function matrix and the MO conductivity matrix. By considering the current-current correlation induced by e-e interaction in the Kubo formula [9, 25, 53, 54], we can calculate the transverse or Hall MO conductivity $\sigma_{xy}(\omega)$, which is the off-diagonal component in MO conductivity matrix. From $\sigma_{xy}(\omega)$, we can obtain the off-diagonal component of the dynamical dielectric function matrix $\epsilon_{xy}(\omega)$ by using the relationship: $\epsilon_{xy}(\omega) = \kappa + i\sigma_{xy}(\omega)/(\epsilon_0\omega)$ with ϵ_0 being the vacuum dielectric constant. However, the calculation of $\sigma_{xy}(\omega)$ by using the Kubo formula requires the considerable further analytical and numerical work and, therefore we do not attempt it in the present study. Furthermore, at present most experiments use circularly polarized light to characterize the ML-TMDs. The left-handed circularly polarized (LHCP) and right-handed circularly polarized (RHCP) MO conductivities $\sigma_{\pm}(\omega)$ can be obtained via the relation: $\sigma_{\pm}(\omega) = \sigma_{xx}(\omega) \pm i\sigma_{xy}(\omega)$.

III. RESULTS AND DISCUSSIONS

In this study, we consider n- and p-type ML-TMDs placed on a ferromagnetic substrate where the proximity-induced exchange interaction is presented. For the calculations, we consider the case of a low temperature $T = 4.2$ K, where the scattering mechanism such as the electron-phonon coupling can be safely ignored and the inelastic electronic scattering for inter-level electronic transition is mainly induced by electron-photon interaction. We take ML-MoS$_2$ an example for the present study. The following material parameters for ML-MoS$_2$ [39, 44, 55, 56] are taken in our numerical calculations: $v_F = 5.3 \times 10^5$ m/s, $\Delta = 0.83$ eV, $\lambda_c = -1.5$ meV, $\lambda_v = 74$ meV, $2d = 1.561$Å, g$_v$ =3.57, and g$'_s$ =0.21. Furthermore, we use the Lorentzian type of LL broadening [57] to replace the δ-function in Eq. (28) through $\delta(x) \to (\Gamma/\pi)/(x^2 + \Gamma^2)$ with Γ being the width of the broadened energy states of the LLs [30, 31]. Γ can be approximately evaluated via [21, 58]: $\Gamma = \alpha_0 B^{1/2}$ with a unit of meV when taking B with a unit of Tesla. In the

present study, we take the relatively small values in order to see more clearly the basic features of the MO absorption spectra in n- and p-type ML-MoS$_2$ in the presence of proximity-induced exchange interaction and external electrical field.

In Fig. 1, we plot the LLs E_α, second-order correction $E_\alpha^{(2)}$ relative to the LLs induced by trigonal warping, and Fermi energy for n- and p-type ML-MoS$_2$ as a function of magnetic field strength B for fixed carrier densities n_β, electrical field strength E_z, and effective Zeeman fields B_c and B_v. We can see that the second-order corrections of LLs are approximately 10^4 times smaller than the LLs in the absence of trigonal warping term. Thus the impact of trigonal warping on the LLs and the position of MO absorption peaks is indeed very small. Meanwhile, the trigonal warping can induces additional allowed transition channels $n \to n \pm 2$ and $n \to n \pm 4$ but the strengthes of new MO absorption peaks would be relatively weak and we can safely ignore it in our following calculations [26]. The energies of LLs in conduction (valence) band increase (decrease) linearly with increasing magnetic field B, which is the common feature of LLs in 2DEG system with parabolic band structure under the action of the perpendicular magnetic field [30, 31, 38]. From Fig. 1, we can see that the LLs in conduction (valence) band in valley K' are higher (lower) than those in valley K. This is because in the presence of proximity-induced exchange interaction and when $B \to 0$, the valley degeneracy in the conduction and valence bands can been lifted [9]. In n-type ML-MoS$_2$ with a fixed electron density $n_+ = 2 \times 10^{12}$ cm^{-2}, the electrons mainly occupy the spin-up LLs, where the full spin-polarization can be always achieved even in large magnetic fields. In contrast, as can be seen from Fig. 1(b), in p-type ML-MoS$_2$ with a low hole density the holes mainly occupy the spin-down LLs, where the full spin-polarization can be achieved in small magnetic fields. We also noted that Ref. [30] investigated the effect of spin and valley Zeeman fields on magneto-transport properties of ML-MoS$_2$ and the lifting of valley degeneracy occurs when the spin and valley Zeeman fields are presented. However, the effective Zeeman fields originated from the proximity-induced exchange interaction can largely enhance the breaking of the spin and valley degeneracies in the presence of a magnetic field which can introduce the large spin and valley polarizations.

In Fig. 2, we plot the LLs of ML-MoS$_2$ in conduction with LL index $n = 1$ and valence bands with LL index $n = 5$ as a function of experienced effective Zeeman field B_c ($B_v = 0$ meV) in (a) and B_v ($B_c = 0$ meV) in (b) at fixed electrical field strength E_z for different magnetic field strengths B to clearly show the influence of proximity-induced exchange interaction on the LLs spectrum of ML-MoS$_2$. We can see that the energies of LLs increases with B_c (B_v) for spin down subbands and decreases with B_c (B_v) for spin up subbands. For a specific experienced effective Zeeman field, we notice that there exist LLs degeneracy as shown by the black circles
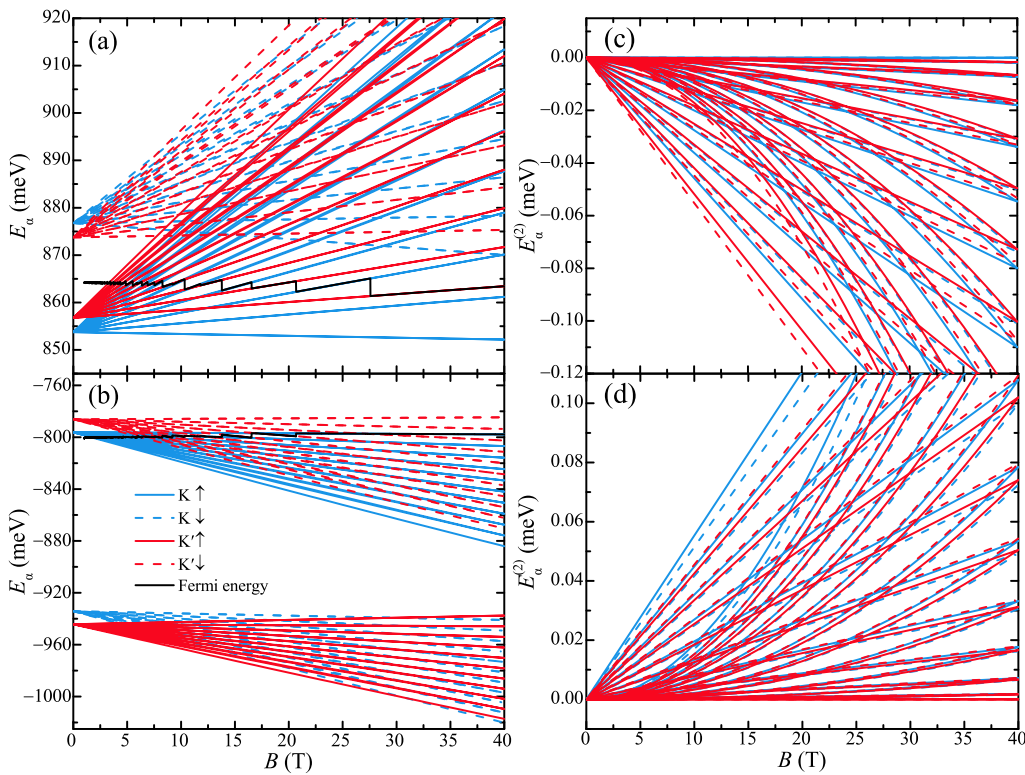
FIG. 1. The LLs E_α (left) and the second-order correction $E_\alpha^{(2)}$ (right) induced by trigonal warping, and Fermi energy (black curves) of n- and p-type ML-MoS$_2$ as a function of magnetic field strength B for fixed carrier density $n_\beta = 2 \times 10^{12}$ cm^{-2}, electrical field strength $E_z = 35.25$ mV/d, effective Zeeman fields $B_c = 10$ meV and $B_v = 5$ meV. (a) and (c) as well as (b) and (d) correspond to the conduction and valence bands, respectively. The spin up/down LLs in K and K' valleys are indicated.

indicated by numbers (1) ∼ (10). At the intersection shown by circle (1), the spin up electrons and the spin down electrons in K' valley are degenerate when $B_c = 1.54$ meV and the energies of spin subbands are reversed with $B_c > 1.54$ meV. Similarly, the same features occur at circles (2) ∼ (10) which indicate that the spin states can be effectively tuned by the proximity-induced interaction. Compared to the conduction band, the valence band requires a larger experienced effective Zeeman fields to achieve the reversals. In addition, with increasing the magnetic field strength B, the locations of the intersections are also shifted. In Fig. 3, we show the schematic illustration of the LLs structure of ML-MoS$_2$ with LL index $n = 0$ at fixed external electrical field strength E_z for different magnetic fields B, experienced effective Zeeman fields B_c and B_v. From the first two columns in Fig. 3(a), we can see that magnetic field can break the energy degeneracy in two valleys. However, this behavior is not obvious in Fig. 3(b) because it needs larger magnetic field in valence band. We find that the LLs splitting increases with increasing the experienced effective Zeeman field B_c (B_v). In Fig. 3(a), with $B_c = 1$ meV, the LLs energy $E_{+0}^{++} < E_{+0}^{--} < E_{+0}^{-+} < E_{+0}^{+-}$, with $B_c = 1.57$ meV, the LLs E_{+0}^{--} and E_{+0}^{-+} are degenerate, with $B_c = 2$ meV, the LLs energy $E_{+0}^{++} < E_{+0}^{-+} < E_{+0}^{--} < E_{+0}^{+-}$, we can see that spin indexes of the spin subbands of LLs

are interchanged at $B_c > 1.54$ meV. Similarly, the same features occur at valence bands in Fig. 3(b). We can obtain that proximity-induced interaction can reverse the spin indexes of the spin subbands of LLs. Moreover, at a magnetic filed $B = 1$ T, the LL E_{+0}^{+-} are lifted with the energy higher than LL E_{+0}^{-+} after applying an experienced effective Zeeman field $B_c = 1$ meV. Thus, the proximity-induced interaction and magnetic field can effectively tune the energies and degeneracy of LLs in ML-MoS$_2$.

In Fig. 4, we plot the spin polarization $\mathcal{S}$ of n-type and p-type ML-MoS$_2$ as a function of total electron (hole) density n_β at fixed external electric field strength, and magnetic field for different experienced effective Zeeman fields. In general, we can see that the absolute value of spin polarization $|\mathcal{S}|$ decreases with increasing carrier density. We can explain the trend of spin polarization in Fig. 4 with the help of Fig. 3. For example, with $B_c = 1$ meV in Fig. 3(a), the LLs energies have the feature of $E_{+0}^{++} < E_{+0}^{--} < E_{+0}^{-+} < E_{+0}^{+-}$. With increasing carrier density, electrons would first fill into the lower spin up subbands E_{+0}^{++} with the 100% spin polarization, and then fill into spin down subbands E_{+0}^{--} with decreasing the spin polarization. We can see that spin polarization has a tendency to increase because the spin up subband E_{+0}^{-+} are filled at this time. With the occupation of electrons to
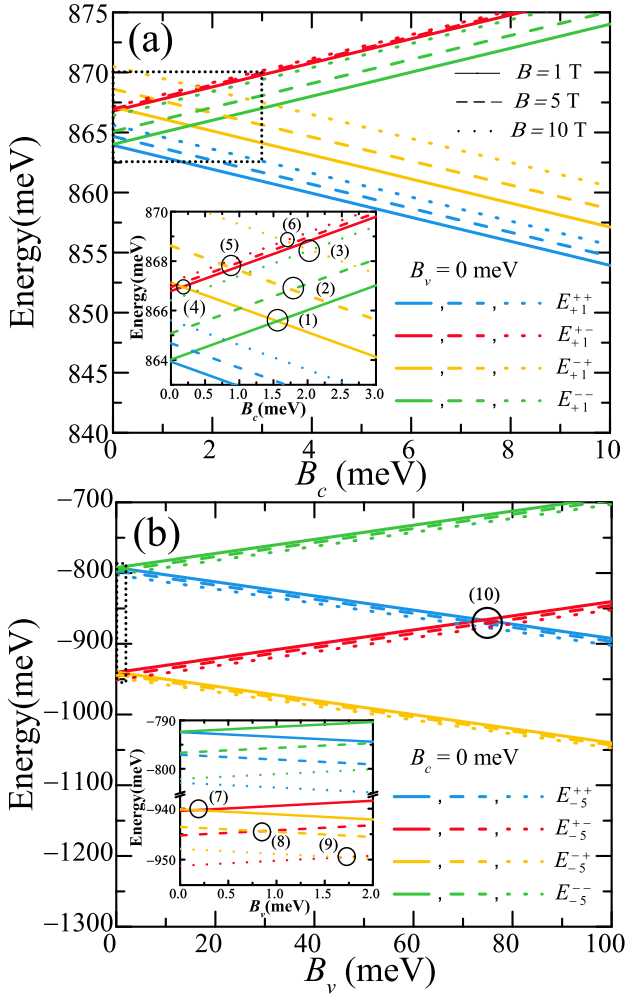
FIG. 2. The LLs $E_{\beta n}^{++}$ (blue), $E_{\beta n}^{+-}$ (red), $E_{\beta n}^{-+}$ (yellow), and $E_{\beta n}^{--}$ (green) in ML-MoS$_2$ in (a) conduction band with LL index $n = 1$ as a function of effective Zeeman fields B_c ($B_v = 0$ meV) and (b) valence band with LL index $n = 5$ as a function of effective Zeeman fields B_v ($B_c = 0$ meV) at the fixed electrical field strength $E_z = 35.25$ mV/d for different magnetic field strengths $B = 1$ (solid line), $B = 5$ (dashed line), and $B = 10$ T (dotted line), respectively. The insets in (a) and (b) are the zooms in of the dotted rectangle areas.

FIG. 3. Schematic illustration of the LLs structure in ML-MoS$_2$ with LL index $n = 0$ at the fixed external electrical field strength $E_z = 35.25$ mV/d for different magnetic fields B, effective Zeeman fields B_c and B_v. The upper panel (a) and lower panel (b) correspond to the conduction and valence bands, respectively.

spin down subband E_{+0}^{+-}, the spin polarization will gradually decreases to zero. For low carrier density, the spin polarization is tortuous because of the overlap between Landau levels. The increasing of the experienced effective Zeeman fields B_c in n-type and B_v in p-type MoS$_2$ can sustain a full spin polarization for a large range of carrier density. For a fixed carrier density, we find that the spin polarization would increases with increasing the effective Zeeman fields. In addition, we find that a small effective Zeeman field factors B_c can achieve a large spin polarization compared to previous studies where a large Rashba parameter is required to achieve spin polarization [9]. From Fig. 4, we obtained that the proximity-induced exchange interaction can effectively tuned the spin po-
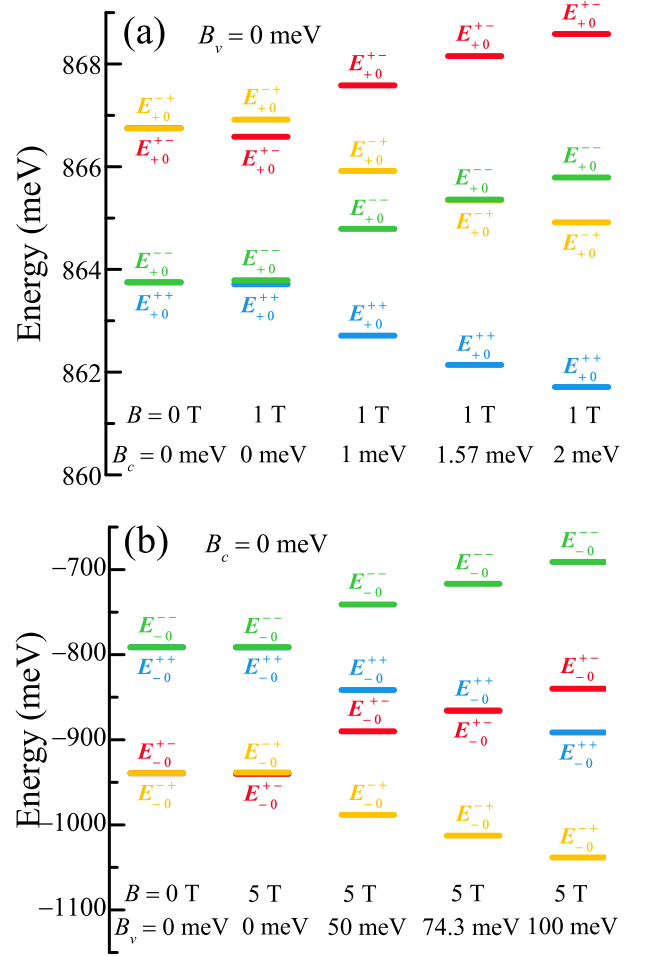
larization of ML-MoS$_2$ under a magnetic field. One can acquire a large spin polarization by the effective Zeeman fields from the proximity-induced exchange interaction.

The MO conductivity $\sigma_{xx}(\omega)$ induced via the electronic transitions within the conduction and valence bands as a function of radiation photon energy $\hbar\omega$ at the fixed carrier densities, external electric field strength, and effective Zeeman field factors for different magnetic field strengths are shown in Fig. 5. As can be seen, there are two absorption peaks in MO conductivity spectrum in the THz regime for both n- and p-type ML-MoS$_2$ with different magnetic fields corresponding to transition energies $\hbar\omega_1 = |E_{\beta n}^{\zeta s} - E_{\beta n \pm 1}^{\zeta s}| \approx \hbar^2 \omega_c^2/(2\Delta_{\zeta s})$. This behavior differs from previous report where only one absorption peak was observed [59, 60]. Such an effect is a consequence of the breaking of the band symmetry in K and K' valleys due to the presence of the proximity-induced exchange interaction. We note that two electronic transi-
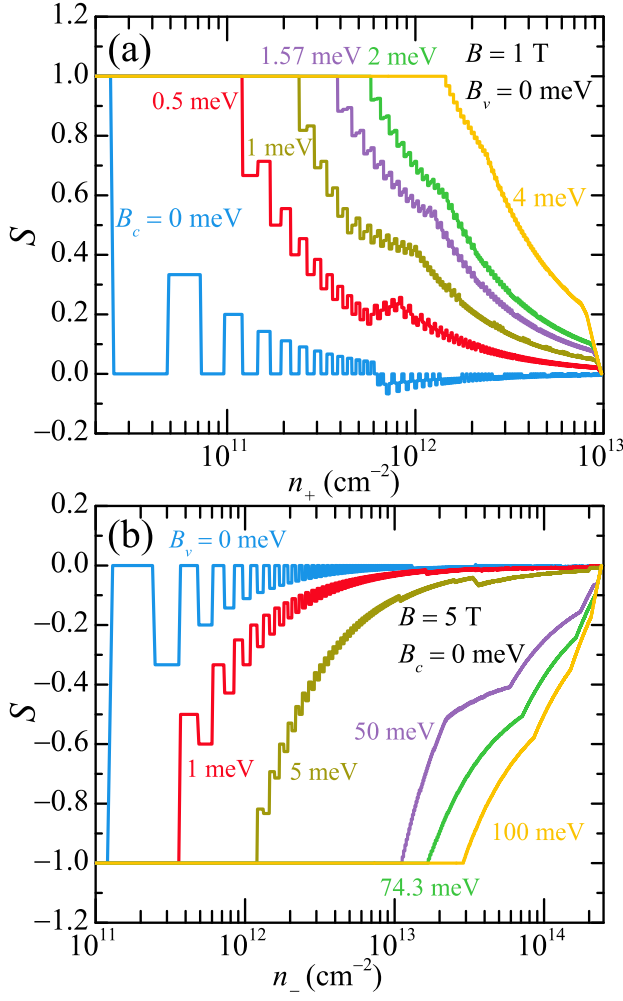
FIG. 4. The spin polarization $\mathcal{S}$ of n-type and p-type ML-MoS$_2$ as a function of electron/hole density n_β at the fixed temperature $T = 0$ K, external electrical field strength E_z = 35.25 mV/d, and magnetic field B for different effective Zeeman fields B_c and B_v. (a) and (b) correspond to the conduction and valence bands, respectively.

tion channels $(\zeta, s, n \rightarrow n')$ contribute to each absorption peak because $\hbar\omega_1$ depends less on LLs index n and the allowed electronic transitions occur only near the Fermi Level (or chemical potential at a finite temperature). For n-type ML-MoS$_2$ in Fig. 5(a), the two absorption peaks are due to the electronic transitions for spin up electrons in valley K' and valley K, respectively. In Fig. 5(b), the first absorption peak in p-type ML-MoS$_2$ is contributed by the electronic transitions for spin down holes in valley K' and the second one relates to the electronic transitions for spin up holes in valley K. These spin and valley dependent electronic transition channels are attributed to the spin and valley polarization caused by the experienced effective Zeeman fields. The energy spacing between two absorption peaks increases with the magnetic field strength, indicating that the MO absorption peaks for different transition channels between LLs can be more
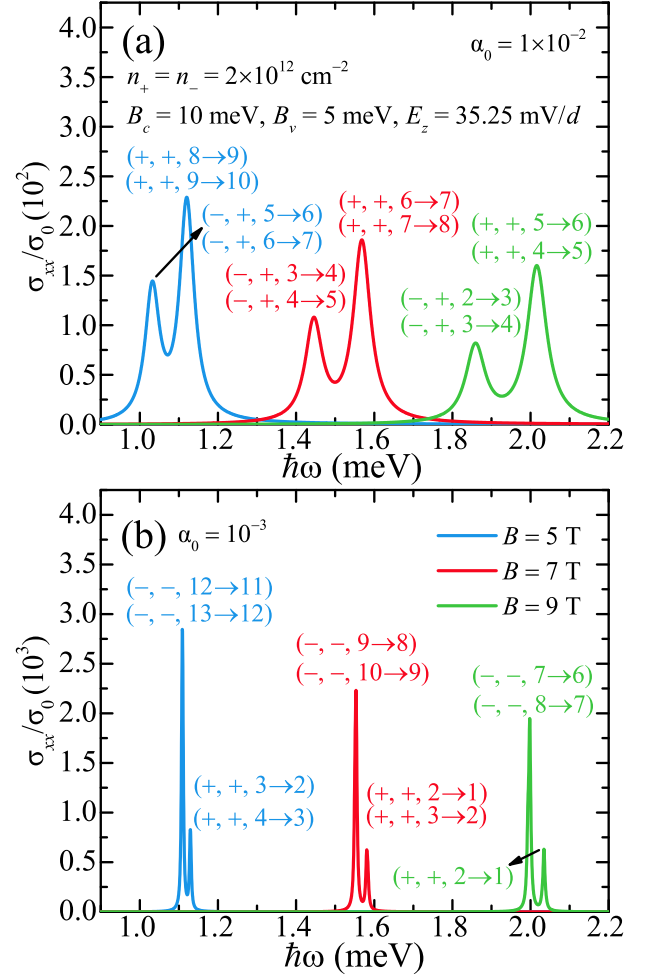

FIG. 5. Magneto-optical conductivity induced via the electronic transition within the conduction bands in (a) and valence bands in (b) in ML-MoS$_2$ as a function of radiation photon energy $\hbar\omega$ at the fixed carrier densities $n_\beta = 2 \times 10^{12}$ cm^{-2}, external electrical field strength E_z = 35.25 mV/d, effective Zeeman field factors B_c = 10 meV and B_v = 5 meV for different magnetic fields $B = 5$ (blue curve), $B = 7$ (red curve), and $B = 9$ T (green curve), respectively. The electronic transition channels corresponding to the absorption peaks are indicated by $(\zeta, s, n \rightarrow n')$. Here $\sigma_0 = e^2/h$.

obviously observed in stronger magnetic field. With increasing magnetic field strength, the absorption peaks in MO conductivity show a blue-shift due to the increase in energy spacing between LLs as shown in Fig. 1.

In Fig. 6, we plot the MO conductivity induced by electronic transitions within the conduction and valence bands of n-type and p-type ML-MoS$_2$ as a function of photon energy $\hbar\omega$ at the fixed carrier densities, external electric field and magnetic fields for different experienced effective Zeeman fields. With increasing experienced effective Zeeman fields B_c and B_v, the MO absorption peaks have blue-shifts for spin down subbands and red-shifts for spin up subbands both in n-type and
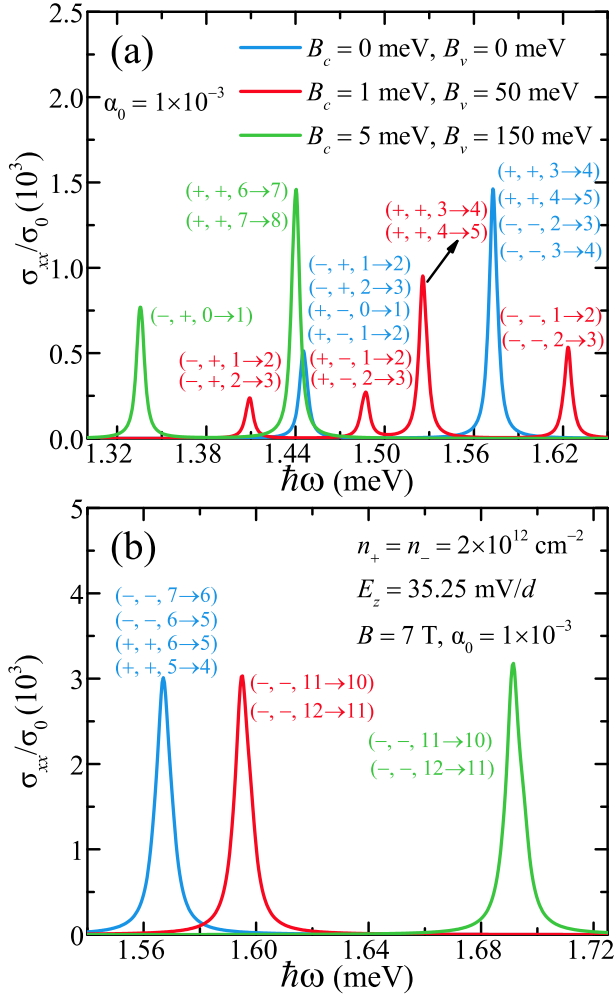
FIG. 6. Magneto-optical conductivity induced by intra-band electronic transition within (a) the conduction band and (b) the valence band as a function of radiation photon energy $\hbar\omega$ at the fixed carrier density n_β, external electrical field strength $E_z = 35.25$ mV/d and magnetic field $B = 7$ T for different effective Zeeman fields $B_c = 0$ meV, $B_v = 0$ meV (blue curve), $B_c = 1$ meV, $B_v = 50$ meV (red curve), and $B_c = 5$ meV, $B_v = 150$ meV (green curve), respectively.

FIG. 7. Magneto-optical conductivity induced by intraband electronic transitions within (a) the conduction band in n-type ML-MoS$_2$ and (b) the valence band in p-type ML-MoS$_2$ as a function of radiation photon energy $\hbar\omega$ at the fixed carrier density $n_\beta = 2.0 \times 10^{12}$ cm^{-2}, effective Zeeman fields $B_c = 10$ meV and $B_v = 5$ meV, and magnetic field $B = 7$ T for different external electrical field strengths $E_z = 35.25$ mV/d (blue curve), $E_z = 70.5$ mV/d (red curve), and $E_z = 105.75$ mV/d (green curve), respectively.

p-type ML-MoS$_2$. We note that the effect of effective Zeeman fields B_c and B_v on LLs are dependent upon the spin index s. Thus the electronic transition energies $\hbar\omega_1 \approx \hbar^2\omega_c^2/(2\Delta_{\zeta s})$ increase for spin down subbands and decrease for spin up subbands with decreasing the value of $B_c - B_v$. And when $B_c \neq 0$, there are more MO absorption peaks, because the proximity-induced interaction can break the band symmetry in K and K' valleys. It should be noted that the experienced effective Zeeman fields B_c and B_v are induced by the proximity-induced interaction which can be different with the choosing of the substrates [9]. Therefore the MO conductivity via the electronic transitions within the conduction and valence bands in THz regime can be effectively tuned by the proximity-induced interaction.
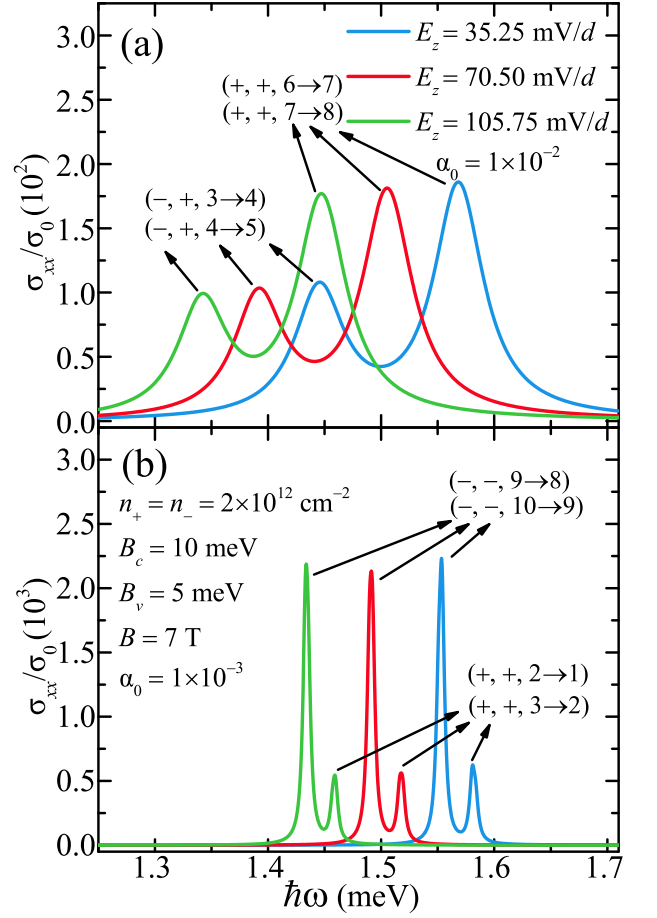
In Fig. 7, we show the MO conductivity induced by electronic transitions within the conduction and valence bands for n-type and p-type ML-MoS$_2$ as a function of radiation photon energy $\hbar\omega$ at the fixed carrier densities, magnetic field, experienced effective Zeeman fields for different external electric field strengths. The increase in the external electric field can lead to lower electronic transition energies $\hbar\omega_1 \approx \hbar^2\omega_c^2/(2\Delta_{\zeta s})$ for both n-type and p-type ML-MoS$_2$. Therefore two MO absorption peaks in Figs. 7(a) and 7(b) show red-shifts with increasing E_z. Consequently, the tuning of the MO absorption can be effectively achieved through applying a perpendicular electrical field. We also plot the MO conductivity caused by electronic transitions within the conduction and valence bands for n-type and p-type ML-MoS$_2$ as a function of radiation photon energy $\hbar\omega$ at the fixed magnetic field, experienced effective Zeeman fields
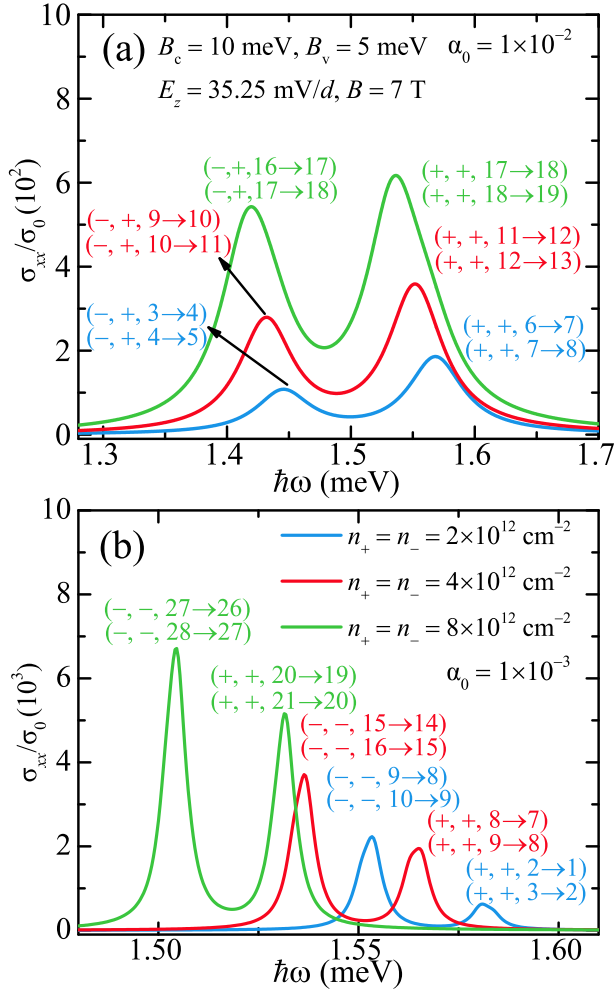
FIG. 8. Magneto-optical conductivity induced by intra-band electronic transitions within (a) the conduction band in n-type ML-MoS$_2$ and (b) the valence band in p-type ML-MoS$_2$ as a function of radiation photon energy $\hbar\omega$ at the fixed effective Zeeman fields $B_c = 10$ meV and $B_v = 5$ meV, external magnetic field $B = 7$ T and external electrical field strength $E_z = 35.25$ mV/d for different carrier densities $n_\beta = 2.0 \times 10^{12}$ cm^{-2} (blue curve), $n_\beta = 4.0 \times 10^{12}$ cm^{-2} (red curve), and $n_\beta = 8.0 \times 10^{12}$ cm^{-2} (green curve), respectively.

and external electric field for different carrier densities in Fig. 8. We can see that two absorption peaks also have red-shifts and the hight of the absorption peaks increase with increasing the carrier density. In Fig. 8, the allowed electronic transitions occur in high index LLs at larger carrier density because the LLs with low index are fully occupied at low temperature. As we known that the carrier density and chemical potential of a 2DEG system can be tuned by, e.g., applying a gate voltage. Thus the MO absorption in ML-MoS$_2$ in THz regime can also be effectively tuned with varying the carrier density.

Different from electronic transitions within the conduction and/or valence bands, which can have two MO absorption peaks in THz frequency regime, the interband
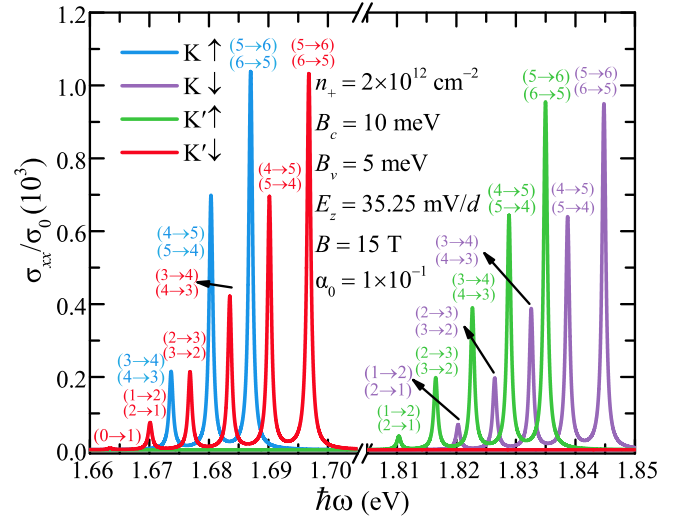

FIG. 9. Magneto-optical conductivity induced by inter-band electronic transitions from valence band to conduction band in n-type ML-MoS$_2$ as a function of radiation photon energy $\hbar\omega$ at the fixed electron density $n_+ = 2 \times 10^{12}$ cm^{-2}, external electrical field strength $E_z = 35.25$ mV/d, effective Zeeman fields $B_c = 10$ meV and $B_v = 5$ meV, and magnetic field $B = 15$ T. The electronic transition channels corresponding to the absorption peaks are indicated by $(\zeta, s, n \to n')$.

electronic transitions among the LLs in the conduction and valence in n-type ML-MoS$_2$ can show a series of MO absorption peaks in visible frequency range owing to the presence of the band gap. In Fig. 9, we plot the MO conductivity for each spin and valley contributed from the first six interband electronic transition channels as a function of radiation photon energy $\hbar\omega$ at the fixed effective Zeeman fields B_c and B_v, magnetic field B, external electrical field strength E_z, and electron density for an n-type ML-MoS$_2$. The photon energies for inter-band transitions between conduction and valence LLs are given by $\hbar\omega_2 = |E_{\beta n}^{\zeta s} - E_{\beta' n \pm 1}^{\zeta s}| \approx (2n+1)\hbar^2\omega_c^2/(2\Delta_{\zeta s}) + 2\Delta_{\zeta s}$, where $n = 0, 1, 2, 3, \cdots$, resulting in a series of absorption peaks in visible range. Besides, with increasing LL index n, the position and the intensity of the absorption peak increases. These results agree with the previous reports for MO response of ML-TMDs [38, 60].

In Fig. 10, we show the total MO conductivity attributed from the first six interband electronic transition channels as a function of radiation photon energies $\hbar\omega$ at the fixed effective Zeeman fields B_c and B_v, external electric field E_z, and electron density with different magnetic fields B for an n-type ML-MoS$_2$. We note that the energy for interband electronic transition $\hbar\omega_2$ increases with the magnetic field strength. Thus the MO absorption peaks move to higher frequency regime with increasing magnetic field strength. This effect can be observed experimentally via, e.g., the visible MO-spectroscopy measurement [61].

The total MO conductivity attributed from the first six interband electronic transition channels as a function of
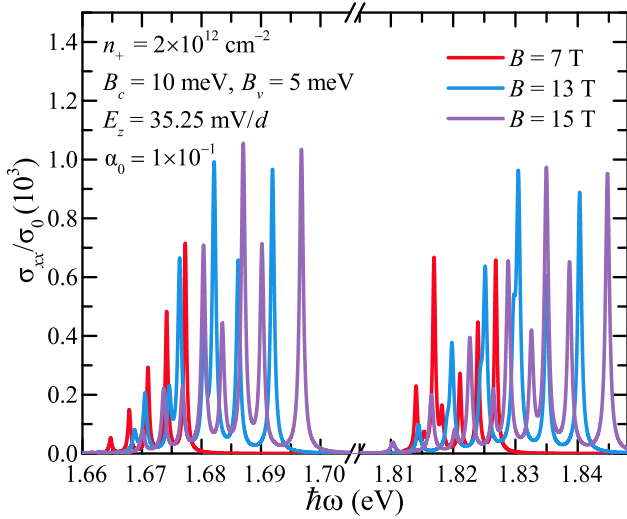
FIG. 10. Magneto-optical conductivity in n-type ML-MoS$_2$ as a function of radiation photon energy $\hbar\omega$ with including the first six interband electronic transition channels at the fixed electron density $n_+ = 2 \times 10^{12}$ cm^{-2}, external electrical field strength $E_z = 35.25$ mV/d, and effective Zeeman fields $B_c = 10$ meV and $B_v = 5$ meV for different magnetic fields $B = 7$ (red curve), $B = 13$ (blue curve), and $B = 15$ T (purple curve), respectively.

FIG. 11. Magneto-optical conductivity in n-type ML-MoS$_2$ as a function of radiation photon energy $\hbar\omega$ with including the first six inter-band electronic transition channels at the fixed electron density $n_+ = 2 \times 10^{12}$ cm^{-2}, external electrical field strength $E_z = 35.25$ mV/d and magnetic fields $B = 15$ T for different effective Zeeman fields $B_c = 10$ meV, $B_v = 5$ meV (red curve), $B_c = 20$ meV, $B_v = 10$ meV (blue curve), and $B_c = 30$ meV, $B_v = 15$ meV (purple curve), respectively.

radiation photon energies $\hbar\omega$ at the fixed external electric field E_z, electron density n_+, and magnetic field B for different effective Zeeman fields B_c and B_v for an n-type ML-MoS$_2$ is shown in Fig. 11. With increasing the value of $B_c - B_v$, we can observe that the MO absorption peaks have both of the blue-shifts and the red-shifts. This phenomena is due to the contributions from different spin subbands at K and K' valleys. We can see that the electronic transition energy $\hbar\omega_2$ increases with $B_c - B_v$ for $s = -1$ and decreases with $B_c - B_v$ for $s = +1$. Thus the blue-shifts are attributed to the electronic transitions of spin-down electrons and the red-shifts are attributed to electronic transitions of spin-up electrons.

In Fig. 12, we show the total MO conductivity induced by the first six interband electronic transitions channels as a function of radiation photon energy $\hbar\omega$ at the fixed electron density, magnetic field strength and effective Zeeman fields B_c and B_v for different external electric field strengths E_z. We find that the MO absorption peaks have blue-shifts with increasing external electric field strength E_z. This is understandable with the help of Eq. (6). The LLs in conduction/valence are higher/lower with increasing external electric field. Hence, the photon energy required for electronic transitions from valence LLs to conduction LLs increases with E_z. By the way, the external electrical field can be easily applied and tuned through a gate voltage in a sample device setup. Thus we can predict that the electrically tunable MO absorptions can be achieved experimentally.

In this study, we theoretically calculate the longitudinal MO conductivity for ML-MoS$_2$ in the presence
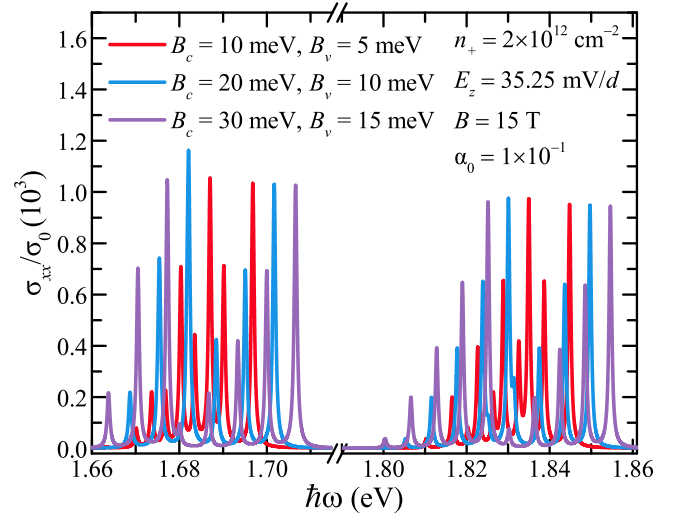
of proximity-induced exchange interaction and external electrical field with the framework of RPA dielectric function. The intraband and interband electronic transitions can be accompanied by the absorption of THz and visible photons. The proximity-induced exchange interaction can breaking the valley degeneracy and result in two MO absorption peaks in THz regime for the intraband electronic transitions within the conduction and/or valence LLs. The electronic transitions from valence LLs to conduction LLs in n-type ML-MoS$_2$ results in a series of MO absorption peaks. Moreover, we find that the proximity-induced exchange interaction, electrical field, carrier density can significantly affect the MO absorption or conductivity in ML-MoS$_2$.

As we know, in the presence of quantizing magnetic fields, the quantum oscillations such as the Shubnikov-de Haas effect and the de Haas-van Alphen effect can be observed in electron gas systems by magneto-transport experiments at low-temperatures. In such case, the oscillations of the longitudinal magneto-resistance/conductance can be measured by varying the B field, where the peak positions correspond to the across of the Fermi energy over the LLs due to the opening up or closing down of the electronic scattering channels. Therefore, the Fermi energy in an electron gas can be evaluated via quantum oscillations observed in magneto-transport measurements [62]. The peaks observed in MO experiments for an electron gas in the presence of quantizing magnetic field at a low-temperature, such as the results shown in this study, are the direct consequence of electronic transitions from occupied LLs to unoccu-
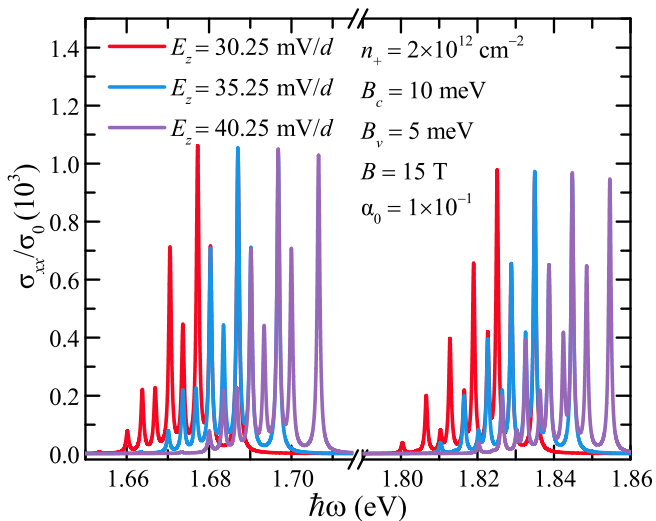
FIG. 12. Magneto-optical conductivity as a function of radiation photon energy $\hbar\omega$ with including the first six interband electronic transition channels at a fixed electron density n_+ $= 2 \times 10^{12}$ cm^{-2}, effective experienced Zeeman fields $B_c = 10$ meV and $B_v = 5$, magnetic field $B = 15$ T for different external electrical field strengths $E_z = 30.25$ mV/d (red curve), $E_z = 35.25$ mV/d (blue curve), and $E_z = 40.25$ mV/d (purple curve), respectively.

pied or empty LLs accompanied by the absorption of the photons. Thus, at a fixed B field, the peak positions in MO absorption spectrum relate to the energy spacings between occupied and unoccupied LLs. By varying the magnetic field, the LL energies should change (see Eq. (6)) so that the peak positions can change in the MO absorption spectrum (see Fig. 10). Meanwhile, the Fermi energy also changes with the B field. It is a fact that the LL occupancy in an electron gas decreases with increasing magnetic field. As a result, when the Fermi energy crosses over a LL by increasing B, some of the MO absorption peaks can disappear owing to the closing down of the allowed optical transition channels. Hence, by monitoring the disappearance of the MO absorption peaks with altering the magnetic field, one can get the information about the Fermi energy in an electron gas in different B fields. Moreover, the main advantage of the MO measurement is that it does not need to fabricate the Hall bar or van de Pauw ohmic contacts on the sample. These contact electrodes are required necessarily for measuring the longitudinal and transverse resistances in conventional magneto-transport experiments. Therefore, the MO experiment is a powerful and practical technique in studying and characterizing the electronic materials and devices. In fact, in recent years the MO absorption spectra have been utilized to probe and manipulate the spin and valley polarized electrons and/or holes in ML-TMD systems [63].

IV. CONCLUSIONS

In this paper, we have presented a detailed theoretical study on Landau level structure and longitudinal magneto-optical conductivity of ML-TMDs in the presence of the proximity-induced exchange interaction and external electrical field. By using the RPA dielectric function for a 2DEG in the presence of quantizing magnetic field, the magneto-optical conductivity has evaluated through the Kubo formula. We have examined the dependence of the MO conductivity or absorption spectrum upon the proximity-induced exchange interaction, carrier density, external electrical filed, and magnetic field in n- and p-type ML-TMDs. The main conclusions obtained from this study can be summarized as follows.

The proximity-induced exchange interaction can break the spin and valley degeneracies in the presence of a magnetic field which can introduce the spin and valley polarizations. The spin and valley dependent electronic transitions can result in two MO absorption peaks in THz regime for the transitions within the conduction or valence LLs. A series of MO absorption peaks can be observed in visible regime, which are attributed from electronic transitions from valence LLs to conduction LLs. In addition, the proximity-induced exchange interaction, carrier density, electrical field, and magnetic field can effectively tune the positions of magneto-optical absorption peaks and modulate the shape of the MO absorption spectrum. Experimentally, the MO absorption of ML-TMDs in visible, infrared and THz ranges can be measured by the techniques such as MO Fourier spectroscopy [61] and MO THz time-domain spectroscopy [64, 65]. Therefore we hope the theoretically findings shown and discussed in this paper can be verified experimentally. It would be promising and interesting to detect the spin and valley polarized electrons or holes through the characteristic magneto-optical absorption peak. The obtained results in this study indicate that ML-TMDs are advanced 2D electronic materials for realizing the magneto-optic, spintronic and valleytronic devices which can work in visible and THz bandwidths. We believe that the results obtained from this work can help us to gain an in-depth understanding of the MO properties of ML-TMDs materials.

[1] K. S. Novoselov, A. K. Geim, S. V. Morozov, D. Jiang, Y. Zhang, S. V. Dubonos, I. V. Grigorieva, and A. A. Firsov, Electric Field Effect in Atomically Thin Carbon Films, Science **306**, 666 (2004).

[2] Q. H. Wang, K. Kalantar-Zadeh, A. Kis, J. N. Coleman, and M. S. Strano, Electronics and optoelectronics of two-dimensional transition metal dichalcogenides, Nat. Nanotechnol. **7**, 699 (2012).

[3] K. F. Mak, C. Lee, J. Hone, J. Shan, and T. F. Heinz, Atomically Thin MoS_2: A New Direct-Gap Semiconductor, Phys. Rev. Lett. **105**, 136805 (2010).

[4] A. Splendiani, L. Sun, Y. Zhang, T. Li, J. Kim, C.-Y. Chim, G. Galli, and F. Wang, Emerging Photoluminescence in Monolayer MoS_2, Nano Lett. **10**, 1271 (2010).

[5] K. F. Mak, K. L. McGill, J. Park, and P. L. McEuen, The valley Hall effect in MoS_2 transistors, Science **344**, 1489 (2014).

[6] Y. M. Xiao, W. Xu, F. M. Peeters, and B. Van Duppen, Multicomponent plasmons in monolayer MoS_2 with circularly polarized optical pumping, Phys. Rev. B **96**, 085405 (2017).

[7] J. Qi, X. Li, Q. Niu, and J. Feng, Giant and tunable valley degeneracy splitting in $MoTe_2$, Phys. Rev. B **92**, 121403(R) (2015).

[8] N. Cortés, F. J. Peña, O. Negrete, and P. Vargas, Proximity-induced spin-polarized magnetocaloric effect in transition metal dichalcogenides, Phys. Rev. B **105**, 014443 (2022).

[9] X. N. Zhao, W. Xu, Y. M. Xiao, J. Liu, B. Van Duppen, and F. M. Peeters, Terahertz optical Hall effect in monolayer MoS_2 in the presence of proximity-induced interactions, Phys. Rev. B **101**, 245412 (2020).

[10] D. Zambrano, P. A. Orellana, L. Rosales, and A. Latgé, Spin and Valley Filter Based on Two-Dimensional WSe_2 Heterostructures, Phys. Rev. Applied **15**, 034069 (2021).

[11] H. Li, Z. Yin, Q. He, H. Li, X. Huang, G. Lu, D. W. H. Fam, A. I. Y. Tok, Q. Zhang, and H. Zhang, Fabrication of Single- and Multilayer MoS_2 Film-Based Field-Effect Transistors for Sensing NO at Room Temperature, Small **8**, 63 (2012).

[12] Z. Yin, H. Li, H. Li, L. Jiang, Y. Shi, Y. Sun, G. Lu, Q. Zhang, X. Chen, and H. Zhang, Single-Layer MoS_2 Phototransistors, ACS Nano **6**, 74 (2012).

[13] B. Radisavljevic and A. Kis, Mobility engineering and a metal-insulator transition in monolayer MoS_2, Nat. Mater. **12**, 815-820 (2013).

[14] B. Radisavljevic, A. Radenovic, J. Brivio, V. Giacometti, and A. Kis, Single-layer MoS_2 transistors, Nat. Nanotechnol. **6**, 147 (2011).

[15] O. Lopez-Sanchez, D. Lembke, M. Kayci, A. Radenovic, and A. Kis, Ultrasensitive photodetectors based on monolayer MoS_2, Nat. Nanotechnol. **8**, 497 (2013).

[16] Y. M. Xiao, W. Xu, B. Van Duppen, and F. M. Peeters, Infrared to terahertz optical conductivity of n-type and p-type monolayer MoS_2 in the presence of Rashba spin-orbit coupling, Phys. Rev. B **94**, 155432 (2016).

[17] A. Ciarrocchi, F. Tagarelli, A. Avsar, and A. Kis, Excitonic devices with van der Waals heterostructures: valleytronics meets twistronics, Nat. Rev. Mater. **7**, 449 (2022).

[18] H. Zeng, J. Dai, W. Yao, D. Xiao, and X. Cui, Valley polarization in MoS_2 monolayers by optical pumping, Nat. Nanotechnol. **7**, 490 (2012).

[19] K. F. Mak, K. He, J. Shan, and T. F. Heinz, Control of valley polarization in monolayer MoS_2 by optical helicity, Nat. Nanotechnol. **7**, 494 (2012).

[20] T. Cao, G. Wang, W. Han, H. Ye, C. Zhu, J. Shi, Q. Niu, P. Tan, E. Wang, B. Liu, and J. Feng, Valley-selective circular dichroism of monolayer molybdenum disulphide, Nat. Commun. **3**, 887 (2012).

[21] T. Ando, A. B. Fowler, and F. Stern, Electronic properties of two-dimensional systems, Rev. Mod. Phys. **54**, 437 (1982).

[22] G. F. Giuliani and G. Vignale, *Quantum theory of the electron liquid*. Cambridge: Cambridge University Press, (2005).

[23] A. H. Castro Neto, F. Guinea, N. M. R. Peres, K. S. Novoselov, and A. K. Geim, The electronic properties of graphene, Rev. Mod. Phys. **81**, 109 (2009).

[24] M. O. Goerbig, Electronic properties of graphene in a strong magnetic field, Rev. Mod. Phys. **83**, 1193 (2011).

[25] C. J. Tabert and E. J. Nicol, Valley-Spin Polarization in the Magneto-Optical Response of Silicene and Other Similar 2D Crystals, Phys. Rev. Lett. **110**, 197402 (2013).

[26] F. Rose, M. O. Goerbig, and F. Piéchon, Spin- and valley-dependent magneto-optical properties of MoS_2, Phys. Rev. B **88**, 125438 (2013).

[27] R. L. Chu, X. Li, S. Wu, Q. Niu, W. Yao, X. Xu, and C. Zhang, Valley-splitting and valley-dependent inter-Landau-level optical transitions in monolayer MoS_2 quantum Hall systems, Phys. Rev. B **90**, 045427 (2014).

[28] A. A. Mitioglu, P. Plochocka, Á. G. del Aguila, P. C. M. Christianen, G. Deligeorgis, S. Anghel, L. Kulyuk, and D. K. Maude, Optical Investigation of Monolayer and Bulk Tungsten Diselenide (WSe_2) in High Magnetic Fields, Nano Lett. **15**, 4387 (2015).

[29] G. Catarina, J. Have, J. Fernández-Rossier, and N. M. R. Peresv, Optical orientation with linearly polarized light in transition metal dichalcogenides, Phys. Rev. B **99**, 125405 (2019).

[30] M. Tahir, P. Vasilopoulos, and F. M. Peeters, Quantum magnetotransport properties of a MoS_2 monolayer, Phys. Rev. B **93**, 035406 (2016).

[31] M. Tahir and P. Vasilopoulos, Magneto-optical transport properties of monolayer WSe_2, Phys. Rev. B **94**, 045415 (2016).

[32] Q. Shi, E.-M. Shih, M. V. Gustafsson, D. A. Rhodes, B. Kim, K. Watanabe, T. Taniguchi, Z. Papić, J. Hone, and C. R. Dean, Odd- and even-denominator fractional quantum Hall states in monolayer WSe_2, Nat. Nanotech. **15**, 569-573 (2020).

[33] R. Pisoni, A. Kormányos, M. Brooks, Z. Lei, P. Back, M. Eich, H. Overweg, Y. Lee, P. Rickhaus, K. Watanabe, T. Taniguchi, A. Imamoglu, G. Burkard, T. Ihn, and K. Ensslin, Interactions and Magnetotransport through Spin-Valley Coupled Landau Levels in Monolayer MoS_2, Phys. Rev. Lett. **121**, 247701 (2018).

[34] T. Smoleński, O. Cotlet, A. Popert, P. Back, Y. Shimazaki, P. Knüppel, N. Dietler, T. Taniguchi, K. Watanabe, M. Kroner, and A. Imamoglu, Interaction-induced

Shubnikov-de Haas oscillations in optical conductivity of monolayer MoSe$_2$, Phys. Rev. Lett. **123**, 097403 (2019).

[35] P. X. Nguyen and W.-K. Tse, Photoinduced anomalous Hall effect in two-dimensional transition metal dichalcogenides, Phys. Rev. B **103**, 125420 (2021).

[36] Z. Li and J. P. Carbotte, Longitudinal and spin-valley Hall optical conductivity in single layer MoS$_2$, Phys. Rev. B **86**, 205425 (2012).

[37] C. V. Nguyen, N. N. Hieu, N. A. Poklonski, V. V. Ilyasov, L. Dinh, T. C. Phong, L. V. Tung, and H. V. Phuc, Magneto-optical transport properties of monolayer MoS$_2$ on polar substrates, Phys. Rev. B **96**, 125411 (2017).

[38] N. D. Hien, C. V. Nguyen, N. N. Hieu, S. S. Kubakaddi, C. A. Duque, M. E. Mora-Ramos, L. Dinh, T. N. Bich, and H. V. Phuc, Magneto-optical transport properties of monolayer transition metal dichalcogenides, Phys. Rev. B **101**, 045424 (2020).

[39] D. Xiao, G.-B. Liu, W. Feng, X. Xu, and W. Yao, Coupled Spin and Valley Physics in Monolayers of MoS$_2$ and Other Group-VI Dichalcogenides, Phys. Rev. Lett. **108**, 196802 (2012).

[40] K. F. Mak, D. Xiao, and J. Shan, Light-valley interactions in 2D semiconductors, Nat. Photon. **12**, 451-460 (2018).

[41] H. Da, L. Gao, W. Ding, and X. Yan, Nonreciprocal Giant Magneto-Optic Effects in Transition-Metal Dichalcogenides without Magnetic Field, J. Phys. Chem. Lett. **8**, 3805-3812 (2017).

[42] H. Ochoa and R. Roldán, Spin-orbit-mediated spin relaxation in monolayer MoS$_2$, Phys. Rev. B **87**, 245421 (2013).

[43] T. Norden, C. Zhao, P. Zhang, R. Sabirianov, A. Petrou, and H. Zeng, Giant valley splitting in monolayer WS$_2$ by magnetic proximity effect, Nat. Commun. **10**, 4163 (2019).

[44] A. Kormányos, V. Zólyomi, N. D. Drummond, and G. Burkard, Spin-Orbit Coupling, Quantum Dots, and Qubits in Monolayer Transition Metal Dichalcogenides, Phys. Rev. X **4**, 011034 (2014).

[45] A. Kormányos, V. Zólyomi, N. D. Drummond, R. Péter, G. Burkard, and V. I. Fal'ko, Monolayer MoS$_2$: Trigonal warping, the Γ valley, and spin-orbit coupling effects, Phys. Rev. B **88**, 045416 (2013).

[46] E. H. Hwang and S. Das Sarma, Dielectric function, screening, and plasmons in two-dimensional graphene, Phys. Rev. B **75**, 205418 (2007).

[47] M. Tahir and K. Sabeeh, Inter-band magnetoplasmons in mono- and bilayer graphene, J. Phys.: Condens. Matter **20**, 425202 (2008).

[48] R. Roldán, M. O. Goerbig, and J.-N. Fuchs, Theory of Bernstein modes in graphene, Phys. Rev. B **83**, 205406 (2011).

[49] W. Xu, Plasmons of a two-dimensional electron gas in the presence of spin orbit interaction, Appl. Phys. Lett. **82**, 724 (2003).

[50] V. N. Kotov, B. Uchoa, V. M. Pereira, F. Guinea, and A. H. Castro Neto, Electron-Electron Interactions in Graphene: Current Status and Perspectives, Rev. Mod. Phys. **84**, 1067 (2012).

[51] M. Tahir and P. Vasilopoulos, Electrically tunable magnetoplasmons in a monolayer of silicene or germanene, J. Phys.: Condens. Matter **27**, 075303 (2015).

[52] C. H. Yang, W. Xu, and C. S. Tang, Fast-electron magneto-optical spectrum of a two-dimensional electron gas in the presence of spin-orbit interaction and quantizing magnetic fields, Phys. Rev. B **76**, 155301 (2007).

[53] V. P. Gusynin, S. G. Sharapov, and J. P. Carbotte, Magneto-optical conductivity in graphene, J. Phys.: Condens. Matter **19**, 026222 (2007).

[54] X. Zhou, W. Chen, and X. Zhu, Anisotropic magneto-optical absorption and linear dichroism in two-dimensional semi-Dirac electron systems, Phys. Rev. B **104**, 235403 (2021).

[55] G.-B. Liu, W.-Y. Shan, Y. Yao, W. Yao, and D. Xiao, Three-band tight-binding model for monolayers of group-VIB transition metal dichalcogenides, Phys. Rev. B **88**, 085433 (2013).

[56] N. Jena, Dimple, S. D. Behere, and A. De Sarkar, Strain Induced Optimization of Nanoelectromechanical Energy Harvesting and Nanopiezotronic Response in MoS$_2$ Monolayer Nanosheet, J. Phys. Chem. C **121**, 9181 (2017).

[57] W. Xu, F. M. Peeters, J. T. Devreese, D. R. Leadley, and R. J. Nicholas, Destrcution of magnetophonon resonance in high magnetic fields from impurity and phonon scattering in Heterojunctions, Int. J. of Mod. Phys. B **10**, 169 (1996).

[58] W. Y. Wang and W. Xu, Magneto-photon-phonon interaction in a parabolically confined quantum dot in the presence of high magnetic fields and intense terahertz radiation fields, Phys. Rev. B **86**, 045307 (2012).

[59] C. V. Nguyen, N. N. Hieu, D. Muoi, C. A. Duque, E. Feddi, H. V. Nguyen, L. T. T. Phuong, B. D. Hoi, and H. V. Phuc, Linear and nonlinear magneto-optical properties of monolayer MoS$_2$, J. Appl. Phys. **123**, 034301 (2018).

[60] P. T. Huong, D. Muoi, T. N. Bich, H. V. Phuc, C. A. Duque, P. T. N. Nguyen, C. V. Nguyen, N. N. Hieu, and L. T. Hoa, Intra- and inter-band magneto-optical absorption in monolayer WS$_2$, Physica E **124**, 114315 (2020).

[61] A. Delhomme, G. Butseraen, B. Zheng, L. Marty, V. Bouchiat, M. R. Molas, A. Pan, K. Watanabe, T. Taniguchi, A. Ouerghi, J. Renard, and C. Faugeras, Magneto-spectroscopy of exciton Rydberg states in a CVD grown WSe$_2$ monolayer, Appl. Phys. Lett. **114**, 232104 (2019).

[62] D. E. Soule, J. W. McClure, and L. B. Smith, Study of the Shubnikov-de Haas effect. Determination of the Fermi surfaces in graphite, Phys. Rev. **124**, A453 (1964).

[63] Z. Wang, J. Shan, and K. F. Mak, Valley- and spin-polarized Landau levels in monolayer WSe$_2$, Nat. Nanotechnol. **12**, 144 (2016).

[64] H. Mei, W. Xu, C. Wang, H. Yuan, C. Zhang, L. Ding, J. Zhang, C. Deng, Y. Wang, and F. M. Peeters, Terahertz magneto-optical properties of bi- and tri-layer graphene, J. Physics: Condens. Matt. **30**, 175701 (2018).

[65] H. Wen, W. Xu, C. Wang, D. Song, H. Mei, J. Zhang, and L. Ding, Magneto-optical properties of monolayer MoS$_2$-SiO$_2$/Si structure measured via terahertz time-domain spectroscopy, Nano Select **2**, 90 (2021).